Research Article | Vol. 14, No. 5 / 1 May 2023 / Biomedical Optics Express 2400
Biomedical Optics EXPRESS

Robustness of the wide-field imaging Mueller polarimetry for brain tissue differentiation and white matter fiber tract identification in a surgery-like environment: an *ex vivo* study

LEONARD FELGER,[1] OMAR RODRÍGUEZ-NÚÑEZ,[1,*] ROMAIN GROS,[2] THEONI MARAGKOU,[2] RICHARD MCKINLEY,[3] STEFANO MORICONI,[3] MICHAEL MUREK,[1] IRENA ZUBAK,[1] TATIANA NOVIKOVA,[4] ANGELO PIERANGELO,[4] AND PHILIPPE SCHUCHT[1]

[1]*Department of Neurosurgery, Inselspital, Bern University Hospital, University of Bern, 3010 Bern, Switzerland*
[2]*Institute of Tissue Medicine and Pathology, University of Bern, 3010 Bern, Switzerland*
[3]*SCAN, University Institute of Diagnostic and Interventional Radiology, Inselspital, Bern University Hospital, University of Bern, 3010 Bern, Switzerland*
[4]*LPICM, CNRS, Ecole polytechnique, IP Paris, 91128 Palaiseau, France*
[*]*omar.rodrigueznunez@insel.ch*

Abstract: During neurooncological surgery, the visual differentiation of healthy and diseased tissue is often challenging. Wide-field imaging Muller polarimetry (IMP) is a promising technique for tissue discrimination and in-plane brain fiber tracking in an interventional setup. However, the intraoperative implementation of IMP requires realizing imaging in the presence of remanent blood, and complex surface topography resulting from the use of an ultrasonic cavitation device. We report on the impact of both factors on the quality of polarimetric images of the surgical resection cavities reproduced in fresh animal cadaveric brains. The robustness of IMP is observed under adverse experimental conditions, suggesting a feasible translation of IMP for *in vivo* neurosurgical applications.

1. Introduction

Malignant tumors of the brain, especially high-grade gliomas (HGG), are among the deadliest tumors known to man, and survival rates are low despite decades of intensive research [1–4]. Surgical resection combined with adjuvant radio-/chemotherapy is the first-line treatment [5–7] for HGG, with the increase in the extent of resection being associated to better patient survival [8–11]. A complete or near total resection is therefore paramount in most cases and remains the neurosurgeon's ultimate goal. However, overly aggressive resection of peritumerous tissue is prone to cause additional and long-lasting or permanent damage to patients' neurological functions, with a negative impact on the patient's quality of life and the prognosis [12].

Therefore, performing surgery on brain tumor patients remains a challenge between too extensive and too little resection. Moreover, the clear identification of brain tumor tissue as well as the surrounding healthy or less severely infiltrated tissue including its potentially eloquent fiber tracts is essential to achieve an optimal clinical outcome. It can be noted that this approach may not only be useful in the detection of brain tumors but also in intraoperative differentiation of other brain tissue pathologies such as injured brain after trauma [13] where the clear differentiation of affected and unaffected tissue is of the essence. Current limitations of modern brain surgery include a poor contrast between the surrounding healthy brain and tumor tissue, as well as the lack of clear intraoperative segmentation of different types of tissue, observed through a

#486438 https://doi.org/10.1364/BOE.486438
Journal © 2023 Received 9 Feb 2023; revised 30 Mar 2023; accepted 1 Apr 2023; published 1 May 2023

Biomedical Optics EXPRESS

white light neurosurgical microscope [14]. Sophisticated methods addressing this challenge are used in standard neurosurgical practice today (Neuronavigation, 5-ALA fluorescence staining, intraoperative MRI) [15,16]. Despite their clear respective benefits, like, for example, increasing the percentage of high grade glioma total resection from 36 to 65 percent only by using 5-ALA fluorescence or making neurosurgery more exact using neuronavigation, these techniques remain either to some extent prone to inaccuracy, inapplicable to all tumors or costly in use, making precise and high contrast intraoperative identification of healthy and diseased tissue an open challenge in modern neurosurgery [17–19]. This emphasizes the clinical need to improve technological solutions that overcome the aforementioned limitations.

Recent studies have shown that the polarimetry-based systems are promising tools for both in- and ex-vivo tissue differentiation and diagnosis [20–29]. Brain polarimetric studies have specifically demonstrated that the strong optical anisotropy of healthy brain white matter (related to the very aligned histological structure of homogeneous nerve fiber bundles and to the presence of axons' myelin sheaths) can be utilized to detect nerve fiber orientation and differentiate it from other brain tissue types [30–35]. This very ordered structure of healthy brain white matter assumed to be altered by brain tumor growth (hypercellularity, hypervascularization, necrosis, break down of fiber arrangement, etc.), producing the changes in the polarimetric response of brain tissue.

We assume that by detecting and characterizing these changes it would be possible to identify and differentiate brain malignancies, not clearly visible to the naked eye. This would overcome the aformentioned limitations, in particular inaccuracy through brain shift as the technique is real time and does not rely on preop imaging and can be applied for all tumor kinds as it is not dependent on the disruption of cellular metabolism. In our prior studies, we demonstrated that the wide-field multispectral IMP system is capable of detecting the in-plane orientation of brain white matter fiber tracts of the flat thick brain specimens in both formalin-fixed or fresh samples, by using polarimetric maps of total depolarization, linear retardance, and azimuth of the optical axis of linear retardance [33–35]. We were also able to differentiate between white and grey matter [33–37].

For intraoperative use the IMP system should ideally be insensitive and robust to the complex and adverse conditions observed during *in vivo* measurements. In [34] we showed that the angle of inclination of the imaged surface (with respect to the probing light beam) in the fresh calf brain tissue samples, as well as the presence of blood in different concentrations and amounts, only marginally affect the polarimetric map of the azimuth of the optical axis of linear retardance generated by our IMP system when measuring the brain specimens with well-defined orientation of fiber tracts.

In this work, we further investigate the robustness of the wide-field IMP system for use in neurosurgery-like conditions, including the complex topography of brain tissue surface, and the presence of irrigation fluids and blood. Tumor resections are typically performed using an Ultrasonic Cavitation and Aspiration Device (UCAD), which is prone to generate an uneven and irregular surface topography in the surgical region of interest [38–41]. Since the UCAD produces local tissue ablation, polarimetric measurements and tissue characterization in reflection configuration might be affected by geometrical distortions of the underlying medium. We therefore examine whether the use of UCAD has an impact on the polarimetric maps of brain tissue, and whether polarimetric tracking of white matter fiber tracts is still feasible in brain tissue exhibiting complex surface topography. Lastly, we also investigate the effects of blood within a resection cavity produced with the UCAD. We use fresh cadaveric animal brains to simulate for the surgical situs where white matter fibers have arbitrary orientation, and the topography of the ablated surface exhibits an irregular pattern.

Biomedical Optics EXPRESS

2. Materials and methods

2.1. Mueller polarimetry: theory and instrument

The most general formalism for describing the interaction of completely or partially polarized light with either non-depolarizing or depolarizing object makes use of the 4 x 4 real-valued Mueller matrix (MM) of an object and four real components of the Stokes vector of a light beam [42–44]. It is possible to access the polarization properties of a sample that are encoded in its MM, provided that each of the combined optical effects can be isolated and quantified. By means of the Lu-Chipman polar decomposition [45] of the measured MM we are able to quantify the depolarization, retardance and diattenuation of a sample.

The depolarization typically occurs because of the loss of coherence when incident polarized light beam is scattered by tissue. The depolarization coefficient is defined as the fraction of unpolarized light in the detected output signal after the interaction of fully polarized incident light with a sample. The retardance describes the effect of birefringence and optical activity that are related to the anisotropy of the refractive index of a medium. The diattenuation arises when the intensity of an object's transmittance/reflectance depends on the polarization state of incident light [42,43,45]. It has already been shown that at normal incidence most of bulk biological tissues exhibits strong depolarization, moderate birefringence, and weak diattenuation [20,37]. The Lu-Chipman decomposition algorithm [45] has been used for the polar decomposition of the measured MM into the product of three matrices for each pixel of the image.

$$\mathbf{M} = \mathbf{M}_{\Delta}\mathbf{M}_{R}\mathbf{M}_{D} \tag{1}$$

where $\mathbf{M}_{\Delta}$, $\mathbf{M}_{R}$ and $\mathbf{M}_{D}$ are the MM of a depolarizer, a retarder and a diattenuator, respectively. In this study, we will focus on the analysis of the total depolarization coefficient Δ, the linear retardance R, and the azimuth φ of the optical axis of the uniaxial linear birefringent medium:

$$\Delta = 1 - \frac{|tr(\mathbf{M}_{\Delta} - 1)|}{3}, 0 \leq \Delta \leq 1 \tag{2}$$

$$R = \arccos\left(\sqrt{(M_R(2,2) + M_R(3,3))^2 + (M_R(3,2) - M_R(2,3))^2} - 1\right) \tag{3}$$

$$\varphi = \frac{1}{2}\arctan\left(\frac{M_R(2,4)}{M_R(4,3)}\right) \tag{4}$$

these parameters have been representative for *ex vivo* brain tissue differentiation so far.

The IMP system described in [25,34,46] is shown in Fig. 1. The instrument is composed of an incoherent white light source, followed by the Polarization State Generator (PSG) for polarization modulation of the incident light beam illuminating the sample. Light, reflected or scattered by the sample, is collected in the detection arm that includes the Polarization State Analyzer (PSA), followed by the spectral filters and the focusing system to generate the image on the CCD-sensor of a camera. The PSG uses an assembly of a linear polarizer, two voltage-driven ferroelectric liquid crystals, and a quarter-wave retarder plate inserted between them, while the PSA is composed of the same components but arranged in the reverse order. The IMP system enables us to obtain a 4 x 4 MM of a sample from the raw intensity data acquired at the chosen wavelength using bandpass filters [46]. The wavelengths of 550 nm and 650 nm were used in a current study. The maps of the depolarization, the scalar retardance, and the azimuth of the optical axis were obtained by applying the Lu-Chipman polar decomposition [45] algorithm to the measured MM images pixel-wise.

2.2. Brain sample preparation

Fresh cadaveric pig brain hemispheres were obtained from a local butcher shop 6 hours post-mortem. The outer layer of the meninges (dura) was removed, the inner layer (Pia) of the

Biomedical Optics EXPRESS

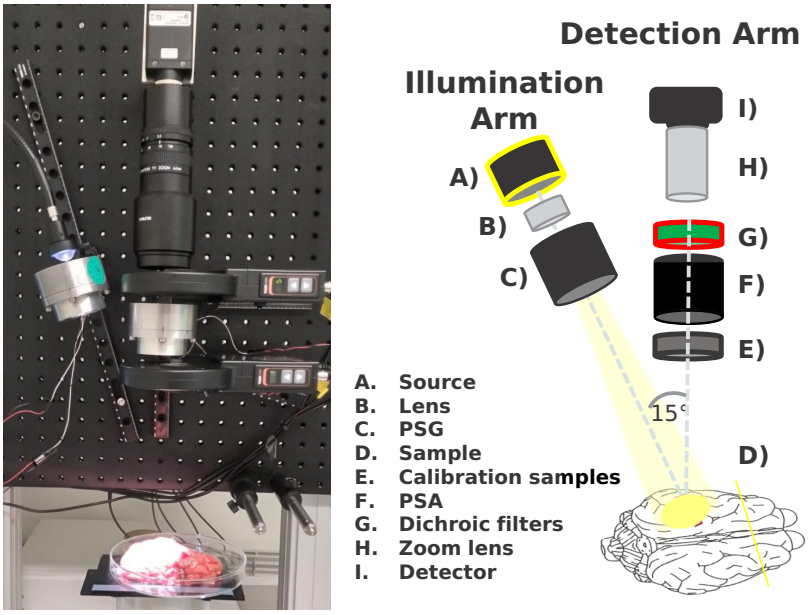

Fig. 1. Wide-field IMP system working in reflection configuration: photo of the instrument (left); schematic of the IMP experimental setup (right). See details in the text.

meninges was preserved covering the brain and the main inter-hemispheric fiber tract (corpus callosum) was severed in the middle. We used two different experimental settings and sample preparation protocols (see Fig. 2) to investigate the effects of UCAD cavitation as well as the robustness of the IMP system.

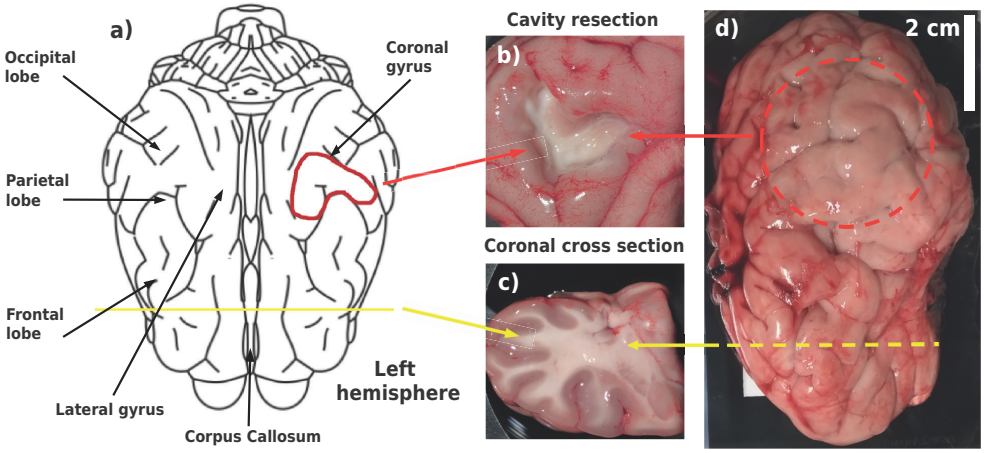

Fig. 2. Brain sample preparation: a) schematic diagram of a pig brain; b) pig brain cavity resection area used after pia mater removal to simulate for a (pseudo-) realistic neurosurgical operation situs, the location of the area is indicated by the solid red line in a) and dashed red line in d); c) coronal cross-section of a cadaveric pig brain, the location of the section is indicated in a) and d) by the solid and dashed yellow lines, respectively; d) top view photo of a fresh pig brain hemisphere.

Biomedical Optics EXPRESS

First, for systematic analysis of the effect of the UCAD on brain tissue polarimetric response, we prepared 1.5 cm thick coronal sections of four pig hemispheres using a large dissection blade (see Fig. 2(c)). After cutting, we selected the sections, which did not include subcortical grey matter structures like basal ganglia for better intra-experimental comparison and clearer macroscopic grey and white matter differentiation (frontal part of the brain, Fig. 2(a)). Thin (~ 1 mm thick) superficial layers of these sections were then removed using the UCAD. The polarimetric measurements were taken before and after the intervention with the UCAD. The detailed process is described in Section 2.3. In a second experiment, to authentically mimic the neurosurgical operating situs we used four entire pig brain hemispheres. We slowly removed the pia mater from the surface of the cortex using forceps and scissors (Fig. 2(d)). We then created a surgical resection cavity of 2.5 cm in depth using the UCAD (see Fig. 2(b)). The layers were removed sequentially until the centrum semiovale was reached. We removed cortical areas only from the visual, auditory and somatosensory cortex for better inter sample comparison. Polarimetric images were taken from the bottom of these cavities as described in Section 2.4.

2.3. Effects of a surgical UCAD: ex vivo studies of coronal cross-section brain tissues

Most tumor resections nowadays are performed using a surgical UCAD. In this work we use the CUSAClarity system from INTEGRA, USA. This device works by disrupting the integrity of biological tissue using a handheld metal tip vibrating at an ultrasonic frequency [38,39]. An integrated irrigation and suction system removes the tissue debris, thus, clearing layer by layer of tissue. The impact of UCAD on the structure of remaining underlying tissue is not well studied. The use of UCAD creates a macroscopically complex surface topography. In order to evaluate the response of the wide-field IMP system operating in reflection mode when imaging the above mentioned cavitated tissue and flat samples with complex surface topography, we examined the effect produced by the UCAD on polarimetric maps of 1.5 cm thick *ex vivo* coronal cross-sections of fresh pig brain prepared as mentioned in section 2.2.

Case I We first obtained the depolarization, the linear retardance, and the azimuth of the optical axis maps of the *ex vivo* coronal sections prepared with a scalpel, using the IMP system over the complete field of view (FoV), the workflow is described in Fig. 3.

Case II We repeat the polarimetric measurements with the same FoV, after removing a brain tissue superficial layer (~1 mm thick), on one half of the sample surface (area 1 in Fig. 3(b)) using the handheld UCAD in vertical stroke motion and low setting.

Case III Finally, the thin surface layer of the other half of the sample surface (area 2 in Fig. 3(b)) was also removed, and the measurement was repeated once again over the complete FoV.

Changes in the orientation of white matter fiber tracts, produced by the intervention with the UCAD, were analyzed by qualitatively comparing the quiver plots of the azimuth of the optical axis before and after the intervention. We compared the complete FoV images for cases I-III. The depolarization and linear retardance maps were first analyzed qualitatively, then we compared quantitatively case I (in-plane surface cut using a blade) and case III (uneven surface with one-millimeter tissue layer removed using the UCAD). For this analysis, two manual masks were first delineated to select the white and grey matter, respectively, from the intensity image, using ImageJ [47]. Then, the histograms of the polarimetric parameters for both case I and case III were plotted to compare the resulting distributions.

2.3.1. Quantitative analysis - before and after intervention

To quantify local changes produced by the UCAD on the coronal section, we performed a comparison of the polarimetric properties over local ROIs in different tissue structures, i.e. in

Biomedical Optics EXPRESS

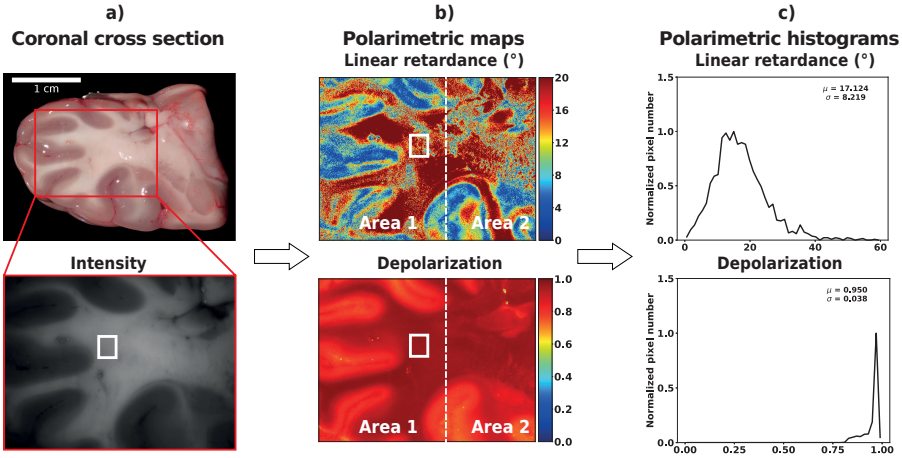

Fig. 3. a) Color photo of a 1.5 cm thick coronal cross-section slice of a cadaveric pig brain (top) and greyscale intensity image of the central zone (2.4 cm × 2 cm) shown by a red rectangle (bottom); b) the maps of the linear retardance (top) and the depolarization (bottom), the areas 1 and 2 are separated by a white dashed line (see Case II); c) an example of the corresponding polarimetric histograms for the region of interest (ROI) shown by a white square of 20×20 pixels (one of 30 manually selected ROIs in the white matter zone). The measurements were performed at the wavelength of 550 nm.

grey and white matter. We evaluated the polarimetric parameters before (case I) and after (case III) the intervention with the UCAD. Reflected intensity images of the same sample were first co-registered between case I and Case III, respectively, with an in-house registration toolbox [48,49]. A series of 30 ROIs of 20 × 20 pixels in the white matter zone and 30 ROIs of the same size in the grey matter zone were automatically and randomly selected for four coronal cross-section slices using the mask manually delineated in the intensity image for case I. Based on the co-registered spatial mapping, the ROIs masks were then propagated from the images for case I to the corresponding images for case III. Spatially inconsistent masks (i. e. the ROIs within either grey or white matter zones in the images for case I, which were translated to the transition zone between grey and white matter in the images for case II) were excluded from the analysis, resulting in an unpaired set of ROIs across brain tissue and considered cases. The mean values of the depolarization and linear retardance were calculated for each ROI and then averaged for white and grey matter zones in the images for case I and case III separately. The statistical differences between the different groups were assessed using Mann–Whitney U test [50].

2.4. Robustness in the surgical resection cavity

2.4.1. Visualization of fibers within the resection cavity

In the next step, we simulated a (pseudo-) realistic neurosurgical operation situs by removing entire gyri from pig brain hemispheres to create resection cavities using the UCAD. An example of the resulting cavity can be seen in Fig. 2(b). Polarimetric maps of depolarization, linear retardance, and azimuth of the optical axis were generated using the MM images acquired with the IMP system, together with the polar decomposition of the recorded MMs for the detection and tracking of brain white matter fibers within the cavity.

Biomedical Optics EXPRESS

2.4.2. Effect of blood presence within the cavities

Lastly, we analyzed the obscuring effect of irrigation fluid and blood on the polarimetric maps by measuring cavities with blood in a diluted (1:5 concentration) water solution using two measurement wavelengths of 550 nm and 650 nm, respectively.

To assess the effect of blood and irrigating fluids presence within the cavity created with the UCAD, we imaged the bottom of the empty cavity in two configurations. First, we acquired the MM images after filling the cavities with the blood/irrigation fluid mixture. Then we acquired the MM images after removing the fluid with the same UCAD used to produce the cavity, leaving small remanent puddles of fluid as in real-case surgical scenarios. To quantify the changes in the maps of the polarimetric parameters related to the presence of blood and irrigation fluid inside the cavity, we manually selected a ROI for the white matter zone within the cavity using intensity images. Histograms of the polarimetric parameters considered in 2.4.1 were obtained for the selected ROI in both configurations.

3. Results

3.1. Effects of the UCAD in coronal cross-section images

The maps of the depolarization, the linear retardance, and the azimuth of the optical axis of a fresh pig brain coronal cross-section are presented in Fig. 4 for the cases I-III described in Section 2.3. These polarimetric maps demonstrate clear contrast between two types of brain tissue in the analyzed samples: white and grey matter from the cerebral coronal section. Qualitatively, the zone of grey matter presents lower depolarization values and lower linear retardance values compared to the corresponding values within white matter zone (Fig. 4). Quantitative analysis of this difference is performed in Section 3.1.1.

From the maps of the azimuth of the optical axis, the orientation of white matter fiber tracts can be recovered for all three cases (see Fig. 4(j-l)). The orientation of the fiber tracts is depicted with the quiver plots and the associated azimuth angles are color-coded. White matter fibers of the superficial in-plane clean cut layer (case I, Fig. 4(j)) reveal a homogeneous spatial orientation pattern associated with either the direction of U-fibers curving around a sulcus (dashed white line from A to B), or corresponding to the direction of the corticospinal fibers (dashed white line from C to D). After partial or total removal of a thin superficial layer of brain tissue using the UCAD, the azimuth map (case II/III, Fig. 4 (k)/(l)) shows local deviations in the orientation of the white matter fibers as underlying differently orientated fibers are being revealed locally. The intensity map (Fig. 4(b), case II) clearly shows the topographic effect produced by the UCAD, which generates an uneven surface of the processed part of a specimen with the removed tissue layer (left) compared to the relatively flat and smooth surface of the unprocessed part of tissue (right).

Despite these local inhomogeneities the fiber tract orientation can still be identified visually in some areas where the in-plane arrangement of the fibers does not change with depth (U-fibers, dashed white line A-B, Fig. 4 (j-l)), whereas whole new underlying fiber bundles running at different crossing directions are revealed elsewhere (dashed white line C-D, Fig. 4 (j-l)). A quantitative analysis of changes in azimuth orientation, however, does not make sense within a specific ROI as this orientation is likely to change after the intervention due to tissue removal.

3.1.1. Polarimetric parameters of brain white and grey matter before and after intervention

To evaluate the impact of the UCAD intervention on the images of the depolarization and linear retardance, we compared the histograms of the parameters in both white and grey matter zones before (case I) and after (case III) ablation (see Fig. 5). The comparison does not reveal significant changes in polarimetric parameter values before and after the ablation of approximately 1 mm of superficial brain tissue. The histograms show that for both depolarization and linear retardance

Biomedical Optics EXPRESS

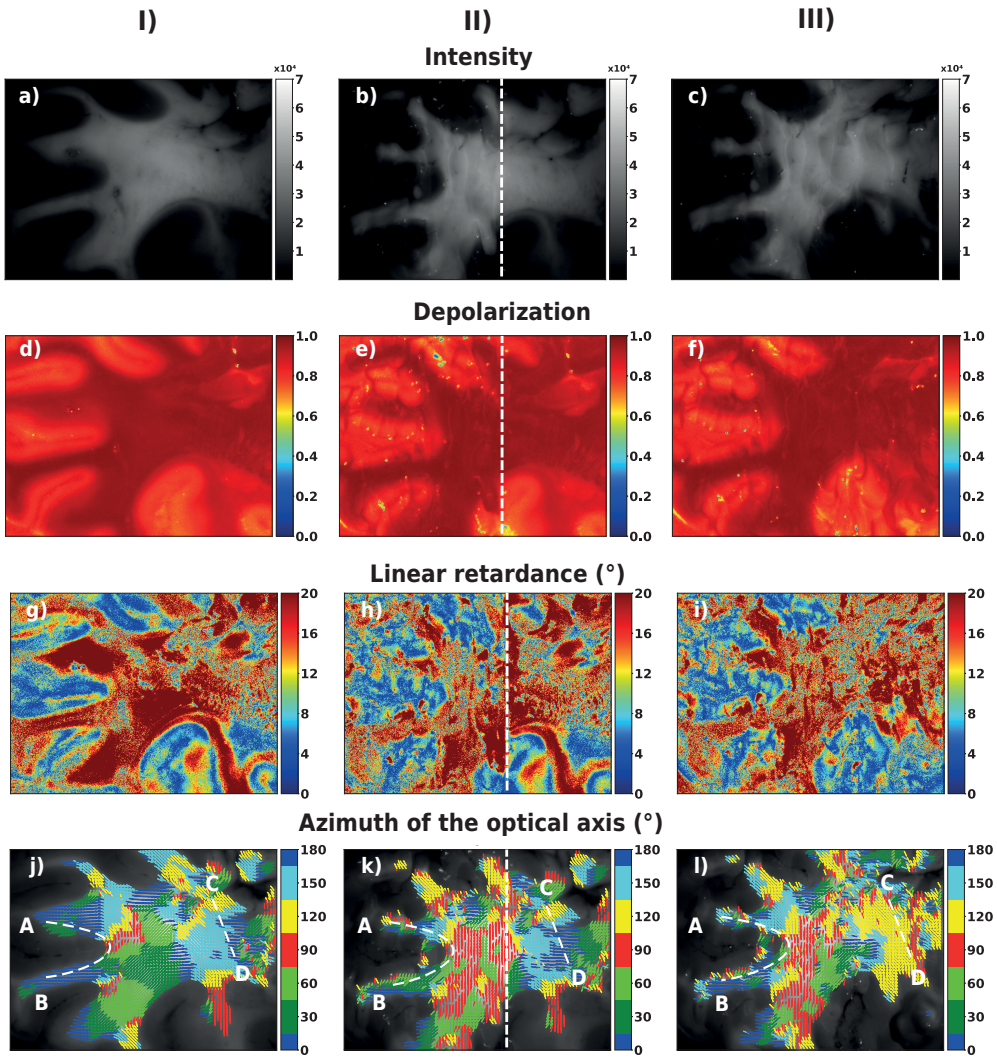

Fig. 4. The images of a coronal cross-section of a cadaveric pig brain: (a), (d), (g) and (j) - case I; (b), (e), (h) and (k) - case II; (c), (f), (i) and (l) - case III. The maps of (a)-(c) intensity; (d)-(f) depolarization, (g)-(i) linear retardance, and (j)-(l) azimuth of the optical axis. A threshold mask (linear retardance >5° and depolarization >90%) was applied to the images of the azimuth of the optical axis in (j)-(l) for the visualization of white matter fibers orientation. All three sets of data were acquired at the wavelength of 550 nm, using the same FoV 2.4 cm × 2 cm.

Biomedical Optics EXPRESS

the mean values for white matter are higher than the mean values for grey matter, for the same specimen.

Changes of the polarimetric parameters in local regions of removed tissue with the UCAD are shown in Fig. 6. The statistical analysis of the observed deviations was performed as described in Section 2.3.1. First, we tested whether the polarimetric parameters were globally altered by the superficial tissue removal with the UCAD. The average of the individual mean values for both depolarization and linear retardance in white matter zone reported higher values compared to grey matter zone values ($p_{value}<1^{-25}$, Mann–Whitney U test) (Fig. 6). Then we examined the local effects of using the UCAD while removing tissue in the specific ROIs. No significant statistical difference (NS) was found for both depolarization in the grey matter and linear retardance in the white matter on a local scale after removing the tissue layer with the surgical aspirator (see Table 1). A significant difference was found when comparing cases I and III for both linear retardance in grey matter (U = 3101, n_1 = 120, n_2 = 117, $p_{value} = 1.1 \times 10^{-2}$, *) and depolarization in white matter (U = 5413, n_1 = 102, n_2 = 76, $p_{value} = 1 \times 10^{-3}$, **). The magnitude of the reported changes was rather small ($10.82° - 9.21° = 1.61°$ and 0.959 - 0.954 = 0.005, respectively), and did not affect the accuracy of the discrimination between white and grey matter. Overall, the observed values of polarimetric parameters remained stable and consistent after removing the layer of brain tissue using the surgical aspirator both locally and on a more global scale.

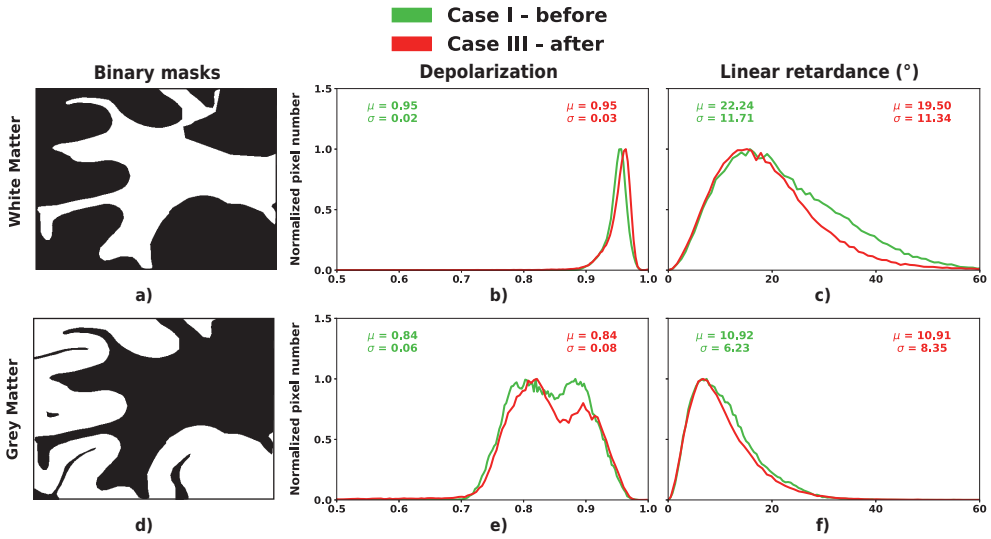

Fig. 5. Analysis of the normalized histograms: (a), (d) - the delineated masks for white and grey matter, respectively, were outlined using ImageJ software based on the intensity image. The pixels rendered in white were considered for analysis, the pixels rendered in black were removed in each case. The histograms of (b),(e) depolarization and (c),(f) linear retardance for white matter (top row) and grey matter (bottom row), case I - green lines, and case III - red lines.

3.2. *Robustness of polarimetric parameters within surgical resection cavity: blood/irrigation fluid experiments*

The intensities and the polarimetric maps of the bloodless cavity obtained with the UCAD are shown in Fig. 7(a) and Fig. 7(c) for both acquisition wavelength of 550 nm and 650 nm, respectively. The depolarization and linear retardance maps showed higher values at the

Biomedical Optics EXPRESS

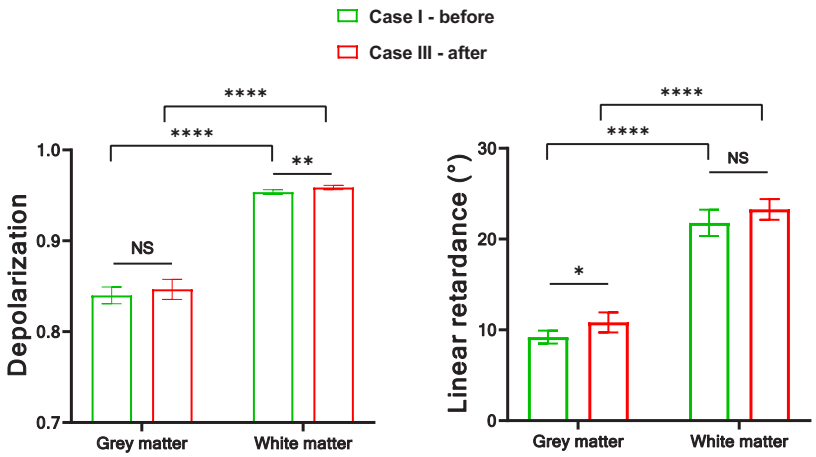

Fig. 6. The average values and 95% confidence interval for the depolarization and linear retardance for local 20 × 20 pixels areas within grey and white matter, respectively, before (case I) and after (case III) superficial tissue removal with the UCAD.

Table 1. Summary of the statistics for the comparison of the polarimetric parameters before and after applying the surgical aspirator for each tissue type. GM - grey matter, WM - white matter of the brain. Parameter n_1 corresponds to the number of ROIs for case I, parameter n_2 - to the number of ROIs for case III.

Parameter	Tissue type	Before	After	U	n_1	n_2	p_{value}
Linear Retardance	GM	9.21 ± 3.60	10.8 ± 4.78	3101	120	117	0.011
Depolarization		0.840 ± 0.047	0.847 ± 0.048	3492	120	117	0.131
Linear Retardance	WM	21.78 ± 7.99	23.27 ± 6.21	6156	102	76	0.051
Depolarization		0.954 ± 0.014	0.959 ± 0.013	5413	102	76	0.001

wavelength of 650 nm compared to the same measurements acquired at 550 nm. The orientation of the white matter fiber tracts within the cavity was correctly recovered as shown in Fig. 7(a) and Fig. 7(c), where directional information is color-coded for the maps of the azimuth of the optical axis. The orientation of the fibers in the left part of the white matter zone ranges between 120° and 160°. Conversely, the fibers in the right part of the white matter zone showed a mainly horizontal orientation at both wavelengths.

In Fig. 7(b) and Fig. 7(d) the effect of remanent blood within the cavity is evaluated following the procedure described in Section 2.4.2. The values of the depolarization and the linear retardance were higher at 650 nm compared to 550 nm wavelength, in presence of remanent blood. The map of the azimuth of the optical axis acquired at 550 nm showed darker areas with remanent blood in Fig. 7(b). This is mainly due to the high blood absorption at the considered wavelength. Conversely, the map of the azimuth acquired at 650 nm (Fig. 7(d)) completely recovered the orientation of the white matter fiber tracts within the cavity, even in presence of remanent blood.

The normalized histograms of depolarization and linear retardance acquired at 550 nm are shown in Fig. 8(a) and Fig. 8(b), respectively. The histograms for the bloodless cavity (green) and the cavity with remanent blood (blue) in Fig. 8 reported similar shapes for the underlying distributions, and the respective mean values for both polarimetric parameters showed minimal deviations. In addition, the histograms of the azimuth of the optical axis at 550 nm (Fig. 8(c)) have a horizontal predominant orientation, these predominant values are associated with and are

Biomedical Optics EXPRESS

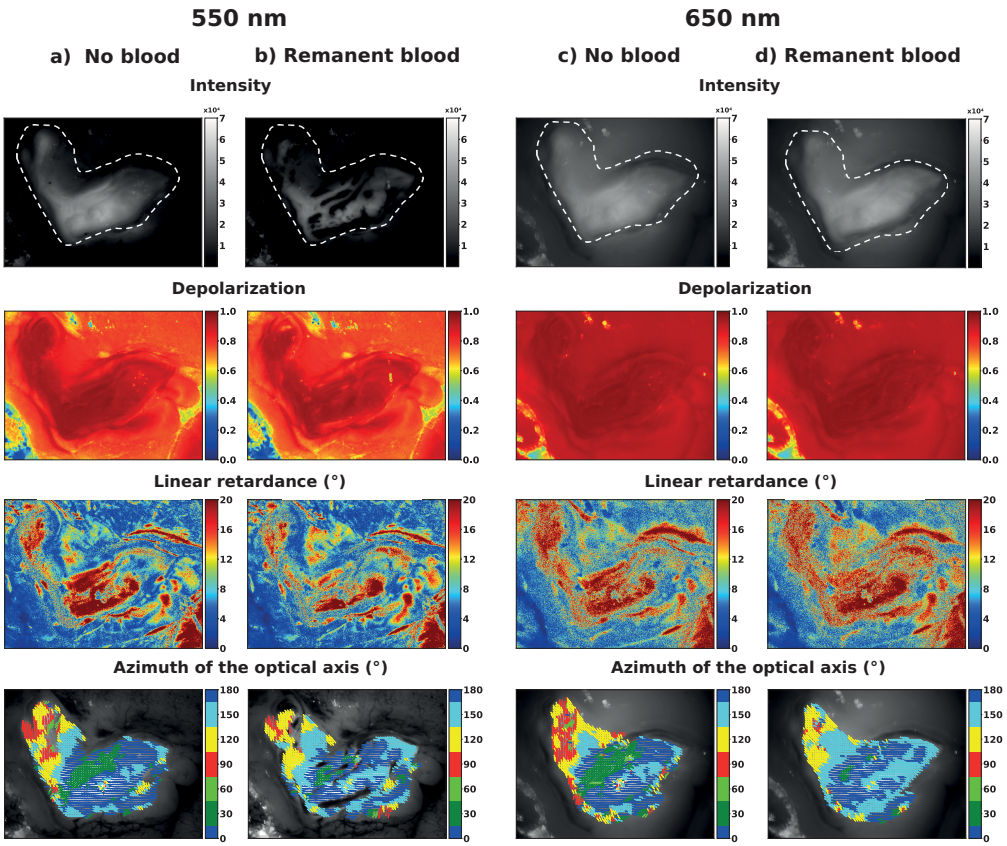

Fig. 7. The images of intensity (first row), depolarization (second row), linear retardance (third row), and azimuth of the optical axis (fourth row) of a pig brain resection cavity produced using the UCAD: (a),(c) bloodless cavity measured at 550 nm and 650 nm, respectively; (b),(d) cavity with remanent blood measured at 550 nm and 650 nm, respectively. The FoV was 2.4 cm×2 cm; a threshold mask (linear retardance >5° and depolarization >90%) was applied to the maps of the azimuth to depict the orientation of the white matter fibers.

consistent with the orientation of the white matter fibers within the cavity, shown in the azimuth maps in Fig. 7(a) and Fig. 7(b).

Similar trends are found for the normalized histograms of the depolarization and linear retardance measured at the wavelength of 650 nm, Fig. 8(d) and Fig. 8(e). In this case, the mean values of the linear retardance histograms differ by about 3 degrees for both cases of bloodless and cavity with remanent blood. The histograms of the azimuth of the optical axis measured at 650 nm (Fig. 8(f)) and associated with the orientation of fibers within the cavity, illustrate the conservation of predominant horizontal orientation of the fibers for both cases with and without remanent blood, which is in agreement with the azimuth maps presented in Fig. 7(c) and Fig. 7(d).

Biomedical Optics EXPRESS

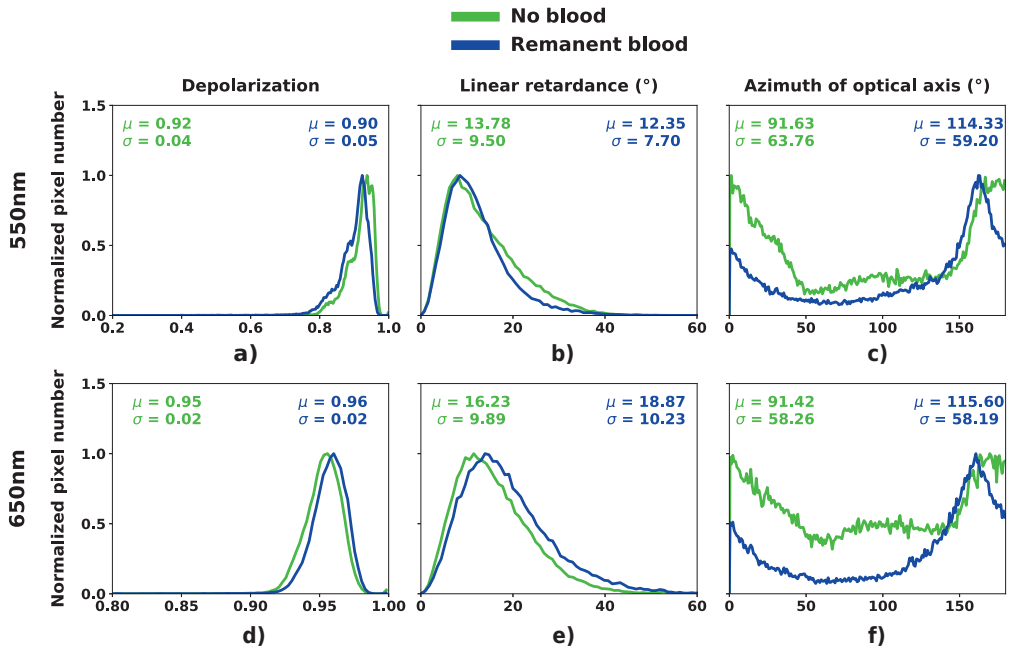

Fig. 8. The normalized histograms of the (a),(d) depolarization; (b),(e) linear retardance: (c),(f) azimuth of the optical axis maps from a pig brain cavity resection measured at the wavelength of 550 nm (top row), and 650 nm (bottom row). Green lines - bloodless cavity, blue lines - the cavity with remanent blood.

4. Discussion

In our first experiment with the IMP system, we measured the polarimetric response (the depolarization, linear retardance and the azimuth of the optical axis) of an in-plane brain specimen and compared it with the response of the same specimen with the uneven surface, after removing a thin layer of tissue with the UCAD.

For cases I-III investigated in Section 3.1, the observed depolarization values are higher for white matter than for grey matter, and such contrast is preserved throughout all the experiments. This is explained by the strong scattering of light within the white matter of brain tissue. It is reasonable that such polarimetric parameter is considered as a good candidate to discriminate among white and grey matter of brain tissue.

The linear retardance, in general, showed higher values in the zone of white matter of brain compared to the linear retardance values in grey matter zone. This can be associated to the presence of dense and aligned white matter fiber bundles that produce a form birefringence and the absence of the fibers structures within grey matter that can be resolved with our wide-field IMP system.

The intensities and polarimetric maps (cases II and III, Fig. 4) showed spatial inhomogeneities after removal a superficial tissue layer with the UCAD, mainly because the UCAD produces local changes to the surface topography of the brain specimen. The histograms in Fig. 5 showed that the local surface inhomogeneities produced by the UCAD do not affect significantly the depolarization and the linear retardance parameters. The corresponding mean values for brain white matter zones remain within the same threshold before and after surgical intervention. Despite a larger pixel-by-pixel variation of parameter values after the intervention, our statistical analysis

Biomedical Optics EXPRESS

suggested the stability of the thresholds for both polarimetric parameters for the delineation of both white and grey matter zones in the images acquired with the IMP system.

The azimuth of the optical axis is an indicator of the orientation of white matter fiber tracts and allows to examine the effects of using a UCAD on fresh animal brain specimens. When the coronal cross-section is cut with a blade one observes very homogeneous brain tissue regions in the maps of the azimuth that correlate well with the orientation of the fiber tracts. In Fig. 4(j-l) local deviations in the orientation of the white matter fibers tracts were observed after removal of a superficial layer of tissue with the UCAD. This result suggests that the thin layer of tissue removed by the UCAD would be revealing new underlying fiber bundles, which become visible to the IMP system. The brain tissue layers were removed sequentially in a vertical direction using the UCAD, and the azimuth maps reported have large areas with clear orientation of brain fibers after UCAD treatment. Because of the physical principles of UCAD operation (i. e. emulsification of the processed tissue), we would expected to see a completely random orientation of azimuth if UCAD treatment affects the underlying fibers, which is not the case in our images. Thus, we believe that the removal of the superficial brain layer with UCAD mainly exposes new fibers and changes the predominant orientation within one pixel according to the underlying micro anatomical grid structure. In addition, the different fiber orientations are consistent from the neuroanatomical point of view, recent studies investigating the microarchitecture and configuration of white matter fibers using high resolution diffusion tensor imaging as well as comparative histology and electron microscopy have revealed a criss crossing configuration of brain axons creating a grid system in which the predominant fiber orientation within a pixel or voxel can potentially change rapidly within short distances [51,52].

Although the UCAD creates an irregular surface, the wide-field IMP system produced the maps of depolarization, linear retardance, and azimuth of the optical axis, which allow the assessment of the structural organization of brain tissue. Therefore, we can discriminate between cerebral white matter and grey matter, and, subsequently, visualize the orientation of the white matter fiber tracts. For fiber tracking in the presence of brain tissue complex topography, the IMP system has been shown to be robust. It is necessary, however, to investigate whether this technique can provide accurate spatial resolution in terms of the penetration depth of light into brain tissue.

In an *in vivo* neurosurgical settings, the IMP system will need to image the cavities with remanent blood that may obscure the tissue to be analyzed. Our results presented in Section 3.2 demonstrate that the presence of blood / irrigating fluids inside the cavity does not affect significantly the quality of polarimetric maps measured inside the cavity at a wavelength of 650 nm, unlike the measurements taken at 550 nm. This was explained by the hemoglobin absorption, which has a peak at 550 nm compared to the low value of the hemoglobin absorption coefficient at 650 nm [53]. Our results are in line with those of our prior studies [34], reporting that the presence of blood in different concentrations on top of the well-ordered fiber tracts of corpus callosum of fresh animal brain does not have a major impact on the values of the polarimetric parameters of brain tissue measured at 650 nm. Compared to [34], the approach discussed in this work goes a step further, since the robustness of the polarimetric parameters measured with the IMP system was demonstrated under the adverse conditions such as irregular surfaces and obstruction of the visual field by blood in cavities, when the tissue was removed with the UCAD.

However, the potential limitations are represented by the physiological pulsation of the brain, which opens up a completely new line of investigation for the *in vivo* application of the IMP system. While a formation of a large pool of blood can be prevented, the motion is ubiquitous in a living organism and can deteriorate the quality of brain images. Brain motion during neurosurgery is not only related to a slow brain shift after opening the skull but also to a continuous and cyclic movement reflecting heart activity. Solutions to overcome this problem have been found for other imaging techniques with long exposure time [54,55], one of those solutions is the use of gated image acquisition, which involves synchronizing image acquisition with the cyclic brain

Biomedical Optics EXPRESS

motion. This approach allows for the acquisition of images only during periods when the sample is relatively stationary, thus reducing the impact of motion artifacts. This has proven to be sufficient in other imaging techniques with long acquisition times i. e. cardiac MRI [54,55].

A further solution to this problem could be shortening the acquisition time. We are currently investigating machine learning techniques which can help to shorten the acquisition time by cleaning up noisy images acquired with a shorter acquisition time. By using deep learning algorithms, it is possible to reconstruct high-quality images from noisy and lower-quality data and reduce the acquisition time. Another approach to shorten acquisition time that is currently under investigation is the incomplete Mueller matrix imaging [56].

5. Conclusion

The wide-field IMP system is a promising tool for brain tissue differentiation and fiber tract visualization for assistance during neurosurgery. In this work we demonstrated that the data acquired with the IMP system working in a reflection configuration are robust and stable under adverse conditions inherent to brain surgery: (i) the resection of brain tissue is performed using the UCAD tool that produces the complex surface topography of a surgical cavity, and (ii) the presence of blood and irrigation fluids in a neurosurgical resection cavity.

The depolarization has been proven to be the most relevant parameter to discriminate between brain white and grey matter. Whereas qualitatively the linear retardance images do not demonstrate the same spatial homogeneity as the images of the depolarization, it was possible to determine statistically that the former shows higher values in white matter zone compared to grey matter tissue before and after the intervention with the surgical aspirator. Additionally, we found a very stable response of the IMP system in terms of detecting the orientation of the white matter fiber tracts before and after the removal of a thin brain tissue layer using the UCAD.

The IMP system employing a broader spectrum of wavelengths proved to be insensitive to possible artifacts introduced by irrigation fluids and remanent blood within a surgical resection cavity. Even when the cavity was created by using the UCAD that produced local inhomogeneities on brain tissue surface and perturbed local fiber orientation, the IMP system was capable to track properly the orientation of the white matter fiber tracts.

Assessing the possible surgical application of an IMP system in reflection configuration in an *ex vivo* model environment, the wide-field IMP system produced robust results on fiber tract visualization under all adverse, neurosurgery-like conditions, taking it one step further as a potential tool for an intra-operative, real-time, non-contact identification of brain tumor borders and brain fiber tract orientation.

Funding. Schweizerischer Nationalfonds zur Förderung der Wissenschaftlichen Forschung (SNF Sinergia grant CRSII5_205904); CONACYT Mexico.

Acknowledgments. O. Rodríguez-Núñez acknowledges the postdoctoral fellowship from CONACYT Mexico.

Disclosures. The authors declare no conflicts of interest.

Data availability. Data underlying the results presented in this paper are not publicly available at this time but may be obtained from the authors upon reasonable request.

References

1. P. Y. Wen and S. Kesari, "Malignant gliomas in adults," N. Engl. J. Med. **359**(5), 492–507 (2008).
2. N. A. Bush, S. M. Chang, and M. S. Berger, "Current and future strategies for treatment of glioma," Neurosurg. Rev. **40**(1), 1–14 (2017).
3. J. N. Cantrell, M. R. Waddle, M. Rotman, J. L. Peterson, H. Ruiz-Garcia, M. G. Heckman, A. Qui nones-Hinojosa, S. S. Rosenfeld, P. D. Brown, and D. M. Trifiletti, "Progress toward long-term survivors of glioblastoma," Mayo Clin. Proc. **94**(7), 1278–1286 (2019).
4. C. L. Pedersen and B. Romner, "Current treatment of low grade astrocytoma: a review," Clin. Neurol. Neurosurg. **115**(1), 1–8 (2013).
5. L. A. Stewart, "Chemotherapy in adult high-grade glioma: a systematic review and meta-analysis of individual patient data from 12 randomised trials," Lancet **359**(9311), 1011–1018 (2002).

Biomedical Optics EXPRESS

6. R. Stupp, W. P. Mason, M. J. van den Bent, M. Weller, B. Fisher, M. J. Taphoorn, K. Belanger, A. A. Brandes, C. Marosi, U. Bogdahn, J. Curschmann, R. C. Janzer, S. K. Ludwin, T. Gorlia, A. Allgeier, D. Lacombe, J. G. Cairncross, E. Eisenhauer, and R. O. Mirimanoff, "Radiotherapy plus concomitant and adjuvant temozolomide for glioblastoma," N. Engl. J. Med. **352**(10), 987–996 (2005).
7. R. Stupp, M. E. Hegi, and W. P. Mason, *et al.*, "Effects of radiotherapy with concomitant and adjuvant temozolomide versus radiotherapy alone on survival in glioblastoma in a randomised phase III study: 5-year analysis of the EORTC-NCIC trial," Lancet Oncol. **10**(5), 459–466 (2009).
8. K. L. Chaichana, E. E. Cabrera-Aldana, I. Jusue-Torres, O. Wijesekera, A. Olivi, M. Rahman, and A. Quinones-Hinojosa, "When gross total resection of a glioblastoma is possible, how much resection should be achieved?" World Neurosurg. **82**(1-2), e257–e265 (2014).
9. O. Bloch, S. J. Han, S. Cha, M. Z. Sun, M. K. Aghi, M. S. Berger, and A. T. Parsa, "Impact of extent of resection for recurrent glioblastoma on overall survival: clinical article," J. Neurosurg. **117**(6), 1032–1038 (2012).
10. N. Sanai and M. S. Berger, "Glioma extent of resection and its impact on patient outcome," Neurosurgery **62**(4), 753–766 (2008).
11. A. W. Awad, M. Karsy, N. Sanai, R. Spetzler, Y. Zhang, Y. Xu, and M. A. Mahan, "Impact of removed tumor volume and location on patient outcome in glioblastoma," J. Neuro-Oncol. **135**(1), 161–171 (2017).
12. M. Rahman, J. Abbatematteo, E. K. De Leo, P. S. Kubilis, S. Vaziri, F. Bova, E. Sayour, D. Mitchell, and A. Quinones-Hinojosa, "The effects of new or worsened postoperative neurological deficits on survival of patients with glioblastoma," J. Neurosurg. **127**(1), 123–131 (2017).
13. H. Zhao, Y. Wang, L. Chen, J. Shi, K. Ma, L. Tang, D. Xu, J. Yao, H. Feng, and T. Chen, "High-sensitivity terahertz imaging of traumatic brain injury in a rat model," J. Biomed. Opt. **23**(03), 1–7 (2018).
14. J. K. W. Gerritsen, M. L. D. Broekman, S. De Vleeschouwer, P. Schucht, B. Vala Nahed, M. Stuart Berger, and A. J. P. Edouard Vincent, "Safe surgery for glioblastoma: Recent advances and modern challenges," Neuro-Oncology Practice **9**(5), 364–379 (2022).
15. A. Naik, E. J. Smith, A. Barreau, M. Nyaeme, S. W. Cramer, D. Najafali, D. T. Krist, P. M. Arnold, and W. Hassaneen, "Comparison of fluorescein sodium, 5-ALA, and intraoperative MRI for resection of high-grade gliomas: A systematic review and network meta-analysis," J. Clin. Neurosci. **98**, 240–247 (2022).
16. W. Stummer, U. Pichlmeier, T. Meinel, O. D. Wiestler, F. Zanella, and H. J. Reulen, "Fluorescence-guided surgery with 5-aminolevulinic acid for resection of malignant glioma: a randomised controlled multicentre phase III trial," Lancet Oncol. **7**(5), 392–401 (2006).
17. I. J. Gerard, M. Kersten-Oertel, K. Petrecca, D. Sirhan, J. A. Hall, and D. L. Collins, "Brain shift in neuronavigation of brain tumors: A review," Med. Image Anal. **35**, 403–420 (2017).
18. P. Abraham, R. Sarkar, M. G. Brandel, A. R. Wali, R. C. Rennert, C. Lopez Ramos, J. Padwal, J. A. Steinberg, D. R. Santiago-Dieppa, V. Cheung, J. S. Pannell, J. D. Murphy, and A. A. Khalessi, "Cost-effectiveness of intraoperative MRI for treatment of high-grade gliomas," Radiology **291**(3), 689–697 (2019).
19. M. S. Eljamel and S. O. Mahboob, "The effectiveness and cost-effectiveness of intraoperative imaging in high-grade glioma resection; a comparative review of intraoperative ALA, fluorescein, ultrasound and MRI," Photodiagn. Photodyn. Ther. **16**, 35–43 (2016).
20. A. Vitkin, N. Ghosh, and A. De Martino, "Tissue polarimetry," in *Photonics: Biomedical Photonics Spectroscopy and Microscopy*, D. L. Andrews, ed. (John Wiley and Sons, Inc., 2015).
21. I. Meglinski, L. Trifonyuk, V. Bachinsky, O. Vanchulyak, B. Bodnar, M. Sidor, O. Dubolazov, A. Ushenko, Y. Ushenko, I. V. Soltys, A. Bykov, B. Hogan, and T. Novikova, *Shedding the Polarized Light on Biological Tissues* (Springer, 2021).
22. J. Qi and D. S. Elson, "Mueller polarimetric imaging for surgical and diagnostic applications: a review," J. Biophotonics **10**(8), 950–982 (2017).
23. H. R. Lee, I. Saytashev, V. N. Du Le, M. Mahendroo, J. C. Ramella-Roman, and T. Novikova, "Mueller matrix imaging for collagen scoring in mice model of pregnancy," Sci. Rep. **11**(1), 15621 (2021).
24. S. Alali and A. Vitkin, "Polarized light imaging in biomedicine: emerging Mueller matrix methodologies for bulk tissue assessment," J. Biomed. Opt. **20**(6), 061104 (2015).
25. T. Novikova, J. Rehbinder, H. Haddad, S. Deby, B. Teig, A. Nazac, A. Pierangelo, F. Moreau, and A. De Martino, "Multi-spectral Mueller matrix imaging polarimetry for studies of human tissue," in *OSA Biophotonics Congress, Clinical and Translational Biophotonics*, vol. TTh3B (2016).
26. J. Vizet, J. Rehbinder, S. Deby, S. Roussel, A. Nazac, R. Soufan, C. Genestie, C. Haie-Meder, H. Fernandez, F. Moreau, and A. Pierangelo, "In vivo imaging of uterine cervix with a Mueller polarimetric colposcope," Sci. Rep. **7**(1), 2471 (2017).
27. A. Pierangelo, S. Manhas, A. Benali, C. Fallet, J. L. Totobenazara, M. R. Antonelli, T. Novikova, B. Gayet, A. De Martino, and P. Validire, "Multispectral Mueller polarimetric imaging detecting residual cancer and cancer regression after neoadjuvant treatment for colorectal carcinomas," J. Biomed. Opt. **18**(4), 046014 (2013).
28. J. Rehbinder, J. Vizet, J. Park, R. Ossikovski, J.-C. Vanel, A. Nazac, and A. Pierangelo, "Depolarization imaging for fast and non-invasive monitoring of cervical microstructure remodeling in vivo during pregnancy," Sci. Rep. **12**(1), 12321 (2022).
29. T. Boonya-ananta, M. Gonzalez, N. V. Du Le, E. DeHoog, M. J. Padidas, A. Jayakumar, and J. C. Ramella-Roman, "A speculum free portable preterm imaging system (PPRIM)," Proc. SPIE **11963**, 119630A (2022).

Biomedical Optics EXPRESS

30. M. Menzel, M. Axer, K. Amunts, H. De Raedt, and K. Michielsen, "Diattenuation Imaging reveals different brain tissue properties," Sci. Rep. **9**(1), 1939 (2019).
31. A. Jain, L. Ulrich, M. Jaeger, P. Schucht, M. Frenz, and H. Günhan Akarcay, "Backscattering polarimetric imaging of the human brain to determine the orientation and degree of alignment of nerve fiber bundles," Biomed. Opt. Express **12**(7), 4452–4466 (2021).
32. M. Borovkova, A. Bykov, A. Popov, A. Pierangelo, T. Novikova, J. Pahnke, and I. Meglinski, "Evaluating β-amyloidosis progression in Alzheimer's disease with Mueller polarimetry," Biomed. Opt. Express **11**(8), 4509–4519 (2020).
33. P. Schucht, H. R. Lee, H. M. Mezouar, E. Hewer, A. Raabe, M. Murek, I. Zubak, J. Goldberg, E. Kovari, A. Pierangelo, and T. Novikova, "Visualization of white matter fiber tracts of brain tissue sections with wide-field imaging mueller polarimetry," IEEE Trans. Med. Imaging **39**(12), 4376–4382 (2020).
34. O. Rodríguez-Nú nez, P. Schucht, E. Hewer, T. Novikova, and A. Pierangelo, "Polarimetric visualization of healthy brain fiber tracts under adverse conditions: ex vivo studies," Biomed. Opt. Express **12**(10), 6674–6685 (2021).
35. T. Novikova, A. Pierangelo, P. Schucht, I. Meglinski, O. Rodríguez-Nú nez, and H. R. Lee, "Mueller polarimetry of brain tissues," in *Polarized Light in Biomedical Imaging and Sensing - Clinical and Preclinical Applications*, J. C. Ramella-Roman and T. Novikova, eds. (Springer Sham, 2023).
36. R. McKinley, L. A. Felger, E. Hewer, T. Maragkou, M. Murek, T. Novikova, O. Rodríguez-Nú nez, A. Pierangelo, and P. Schucht, "Machine learning for white matter fibre tract visualization in the human brain via Mueller matrix polarimetric data," Proc. SPIE **12136**, 121360G (2022).
37. O. Rodríguez-Nú nez and T. Novikova, "Polarimetric techniques for the structural studies and diagnosis of brain," Adv. Opt. Technol. **11**(5-6), 157–171 (2022).
38. E. Kimmel, "Cavitation bioeffects," Crit. Rev. Biomed. Eng. **34**(2), 105–162 (2006).
39. L. J. Bond and W. W. Cimino, "Physics of ultrasonic surgery using tissue fragmentation," Ultrasonics **34**(2-5), 579–585 (1996).
40. F. Ebel, L. Greuter, R. Guzman, and J. Soleman, "Resection of brain lesions with a neuroendoscopic ultrasonic aspirator - a systematic literature review," Neurosurg. Rev. **45**(5), 3109–3118 (2022).
41. E. S. Flamm, J. Ransohoff, D. Wuchinich, and A. Broadwin, "Preliminary experience with ultrasonic aspiration in neurosurgery," Neurosurgery **2**(3), 240–245 (1978).
42. D. Goldstein, *Polarized Light* (Marcel Dekker, 2003), 2nd ed.
43. R. M. A. Azzam, "Stokes-vector and Mueller-matrix polarimetry,," J. Opt. Soc. Am. **33**(7), 1396–1408 (2016).
44. T. Novikova and J. C. Ramella-Roman, "Polarized light," in *Polarized Light in Biomedical Imaging and Sensing - Clinical and Preclinical Applications*, J. C. Ramella-Roman and T. Novikova, eds. (Springer Sham, 2023).
45. S. Y. Lu and R. A. Chipman, "Interpretation of Mueller matrices based on polar decomposition," J. Opt. Soc. Am. **13**(5), 1106–1113 (1996).
46. A. Lindberg, J. Vizet, J. Rehbinder, C. Gennet, J.-C. Vanel, and A. Pierangelo, "Innovative integrated numerical-experimental method for high-performance multispectral Mueller polarimeters based on ferroelectric liquid crystals," Appl. Opt. **58**(19), 5187 (2019).
47. C. A. Schneider, W. S. Rasband, and K. W. Eliceiri, "NIH Image to ImageJ: 25 years of image analysis," Nat. Methods **9**(7), 671–675 (2012).
48. S. Klein, M. Staring, K. Murphy, M. A. Viergever, and J. P. W. Pluim, "Elastix: a toolbox for intensity-based medical image registration," IEEE Trans. Med. Imaging **29**(1), 196–205 (2010).
49. D. Shamonin, "Fast parallel image registration on CPU and GPU for diagnostic classification of Alzheimer's disease," Frontiers in Neuroinformatics **7**, 50 (2014).
50. P. Virtanen, R. Gommers, T. E. Oliphant, and SciPy 1.0 Contributors, *et al.*, "SciPy 1.0: fundamental algorithms for scientific computing in Python," Nat. Methods **17**(3), 261–272 (2020).
51. V. J. Wedeen, D. L. Rosene, R. Wang, G. Dai, F. Mortazavi, P. Hagmann, J. H. Kaas, and W. Y. Tseng, "The geometric structure of the brain fiber pathways," Science **335**(6076), 1628–1634 (2012).
52. K. G. Schilling, V. Janve, Y. Gao, I. Stepniewska, B. A. Landman, and A. W. Anderson, "Histological validation of diffusion MRI fiber orientation distributions and dispersion," NeuroImage **165**, 200–221 (2018).
53. S. Prahl, "Optical absorption of hemoglobin," Online: http://omlc.ogi.edu/spectra/hemoglobin/ (1999).
54. A. Almudayni, M. Alharbi, A. Chowdhury, J. Ince, F. Alablani, L.-V. A. , S. J. , and L. C. E. M. , "Magnetic resonance imaging of the pulsing brain: a systematic review," Magn. Reson. Mater. Phy., Biology and Medicine **36**(1), 3–14 (2022).
55. R. L. Ehman, M. T. McNamara, M. Pallack, H. Hricak, and C. B. Higgins, "Magnetic resonance imaging with respiratory gating: techniques and adavantages," Am. J. Roentgenol. **143**(6), 1175–1182 (1984).
56. T. Novikova and J. C. Ramella-Roman, "Is a complete Mueller matrix necessary in biomedical imaging?" Opt. Lett. **47**(21), 5549–5552 (2022).